Biomaterials
Science

ROYAL SOCIETY
OF CHEMISTRY

PAPER

View Article Online
View Journal | View Issue

Check for updates

Cite this: *Biomater. Sci.*, 2023, **11**, 4549

Iron oxide-EDTA nanoparticles for chelation-enhanced chemodynamic therapy and ion interference therapy†

Changxiao Chen,[a,b] Qi Meng,[a,b] Zhendong Liu,[a,b] Sainan Liu, [a] Weifang Tong,[c] Baichao An,[d,e] Binbin Ding,*[a] Ping'an Ma *[a,b] and Jun Lin *[a,b]

Received 2nd March 2023,
Accepted 23rd April 2023

DOI: 10.1039/d3bm00371j

rsc.li/biomaterials-science

As an emerging anti-tumor strategy, chemodynamic therapy (CDT) utilizes a Fenton/Fenton-like reaction to generate highly toxic hydroxyl radicals to kill tumor cells. However, the efficiency of CDT is still hindered by the low Fenton/Fenton-like reaction rate. Herein, we report the combination of ion interference therapy (IIT) and chemodynamic therapy (CDT) *via* an amorphous iron oxide (AIO) nanomedicine with encapsulated EDTA-2Na (EDTA). Iron ions and EDTA are released from the nanomedicine in acidic tumors and chelate to form iron ion-EDTA, which improves the efficiency of CDT and promotes the generation of reactive oxygen species (ROS). In addition, EDTA can disrupt the homeostasis of Ca^{2+} in tumor cells by chelating with Ca^{2+} ions, which induces the separation of tumor cells and affects normal physiological activities. Both *in vitro* and *in vivo* experiments show that the nano chelating drugs exhibit significant improvement in Fenton reaction performance and excellent anti-tumor activity. This study based on chelation provides a new idea for designing efficient catalysts to enhance the Fenton reaction and provides more revelations on future research on CDT.

Introduction

Cancer is one of the greatest dangers to the health of human beings, and causes nearly 10 million deaths every year.[1,2] Chemodynamic therapy (CDT) is a new type of anti-tumor strategy, which produces reactive oxygen species (ROS) at the tumor site through Fenton/Fenton-like reactions to achieve the effect of killing tumors.[3,4] Due to the properties of the tumor microenvironment (TME, mainly including acidity, higher concentrations of H_2O_2 and so on), CDT is characterized by high selectivity and it is particularly suitable for the treatment of tumors in deep tissues. Nevertheless, with the development of CDT, it also faces the following problems: (1) low Fenton/Fenton-like reaction efficiency, (2) harsh reaction conditions, (3) lack of reaction substrates, and (4) the existence of antioxidant mechanisms in tumor cells, which severely limit the application of CDT.[5] So far, many research studies have been conducted to enhance the effect of CDT,[6–9] whereas few have been used to enhance the Fenton reaction using Fenton's reagent. It has been found that a suitable chelate can effectively enhance the reactivity of the Fenton reaction.[10–13] In addition, by choosing different chelators, the resulting chelates have different effects, such as regulating particle size,[14,15] enhancing the chemotherapeutic efficacy[16,17] and expanding the pH range of the Fenton reaction.[18] Inspired by this, we tried to use this strategy to build a suitable nanoplatform for elevated CDT efficiency. EDTA is a common and significant chelating agent that is widely used in various fields.[12,19] It has been proved that EDTA can be used to dissociate cells by chelating Ca^{2+} to disrupt calcium-dependent proteins.[20–22] In addition, on account of the important physiological significance of Ca^{2+} ions in tumor cells, EDTA can regulate the intracellular Ca^{2+} ion concentration, thereby affecting the normal physiological activities of tumor cells.[23–26]

In this work, a highly effective endogenously enhanced CDT in combination with ion interference therapy (IIT) is proposed. First, amorphous iron oxide (AIO) was selected as the carrier due to its small size and generation of highly reactive hydroxyl radicals ($^{\bullet}OH$).[3,27,28] Next, we prepared AIO-EDTA (EDTA-2Na encapsulated in AIO) nanoparticles (NPs) in one step by a rapid reverse microemulsion method. Benefiting from the chelation of iron ions with EDTA, AIO-EDTA NPs further efficiently catalyze the Fenton reac-

---

[a] *State Key Laboratory of Rare Earth Resource Utilization, Changchun Institute of Applied Chemistry, Chinese Academy of Sciences, Changchun, 130022, China. E-mail: bbding@ciac.ac.cn, mapa675@ciac.ac.cn, jlin@ciac.ac.cn*

[b] *School of Applied Chemistry and Engineering, University of Science and Technology of China, Hefei 230026, China*

[c] *Department of Otolaryngology Head and Neck Surgery, The Second Hospital, Jilin University, Changchun 130041, China*

[d] *College of Pharmacy, Guangdong Medical University, Dongguan 523808, China*

[e] *School of Traditional Chinese Medicine, Southern Medical University, Guangzhou 510515, China*

† Electronic supplementary information (ESI) available: XPS spectra, zeta potentials, DLS results, detection of extracellular Ca^{2+}, cell viability test, images of H&E stained slices, *etc*. See DOI: **https://doi.org/10.1039/d3bm00371j**

tion to promote the generation of $^{\bullet}$OH. Simultaneously, EDTA chelates intracellular and extracellular Ca^{2+} ions to disrupt the homeostasis of Ca^{2+}, achieving the combined treatment of IIT and CDT. Both *in vitro* and *in vivo* consequences have verified the remarkably enhanced therapeutic efficacy of AIO-EDTA compared with AIO and EDTA alone, which provided a new idea for improving Fenton's reagent to enhance CDT and designing nano chelating drugs.

Experimental

Synthesis of AIO-EDTA

12.5 mL of *n*-dodecane, 1.25 mL of 1-hexanol, 455 mg of CTAB and 0.5 mL of an aqueous solution of ethylenediaminetetraacetic acid disodium salt (EDTA-2Na, 15 mg mL^{-1}) were added to a 50 mL glass bottle. After stirring for 15 min to form a reverse microemulsion, 50 μL of H_2O_2 was added. Then, 0.5 mL of $Fe(CO)_5$ was injected into the solution immediately and the solution was stirred at room temperature (RT) for 10 min. Then, 2.5 mL of diethylene glycol was added, and the product was collected by centrifugation (10 000 rpm, 15 min) and washed three times with alcohol.

Lipid PEG coating of AIO-EDTA NPs

Briefly, AIO-EDTA NPs dispersed in ethanol were slowly added to the $DSPE\text{-}PEG_{2000}\text{-}NH_2$ aqueous solution (1 mg mL^{-1}), and the reaction was allowed to proceed for 10 min under moderate stirring. The lipid PEG-coated NPs were isolated by centrifugation and washed twice with water.

Intracellular calcium ion detection

First, 4T1 cells were seeded in 6-well culture plates at a density of 1.5×10^6 cells per well and treated with (a) PBS, (b) EDTA-2Na (5 μg mL^{-1}), (c) AIO NPs (62.5 μg mL^{-1} AIO), and (d) AIO-EDTA NPs (62.5 μg mL^{-1} AIO), respectively. After 4 h of incubation in the dark, the cells were washed three times with PBS. Then, Fluo-4 acetoxymethyl ester (Fluo-4 AM) dispersed in PBS was added and the mixture was incubated for 30 min at 37 °C. Next, the cells were washed three times with PBS and incubated for 20 minutes in the dark. Finally, the fluorescence from Fluo-4 was detected using a fluorescence inversion microscope system.

Extracellular calcium ion detection

First, 4T1 cells were seeded in 6-well culture plates at a density of 1.5×10^6 cells per well. Before the addition of drugs, the cells were washed twice with PBS. The cells were incubated with (a) PBS, (b) EDTA-2Na (5 μg mL^{-1}), (c) AIO NPs (62.5 μg mL^{-1} AIO), and (d) AIO-EDTA NPs (62.5 μg mL^{-1} AIO) for 4 hours in the dark. The supernatant was collected for measurement of calcium ion concentration by ICP.

Results and discussion

Synthesis and characterizations of AIO and AIO-EDTA

A reverse microemulsion method was used to synthesize AIO and AIO-EDTA NPs according to the literature,[27] which is shown in Fig. 1. The as-synthesized AIO-EDTA NPs have similar particles with an average size of 10 nm, as observed by

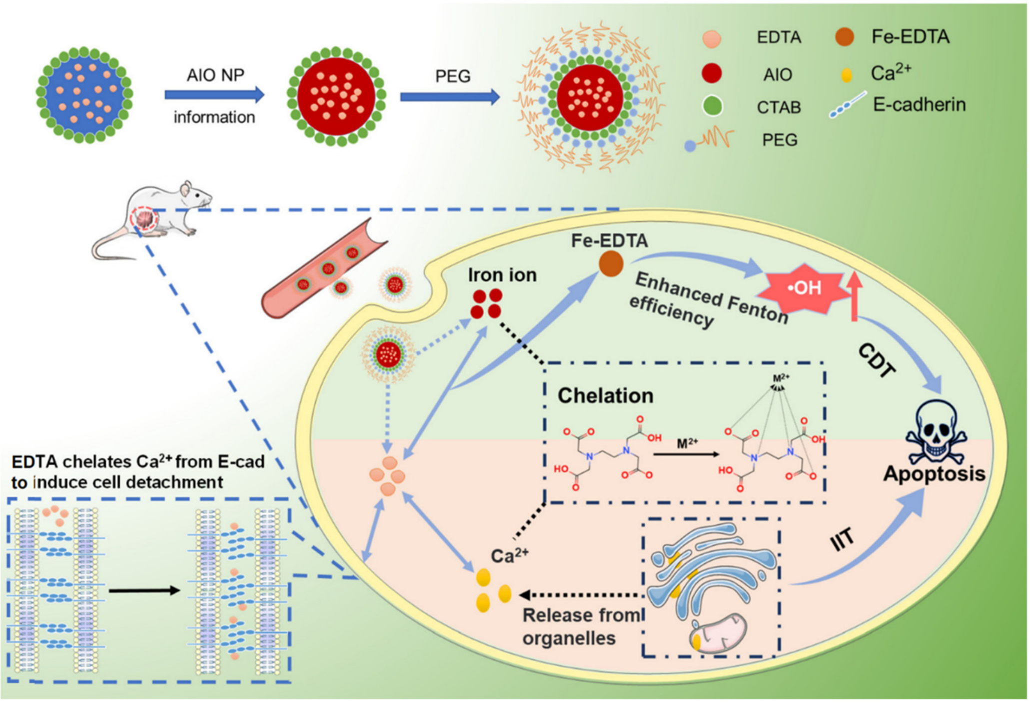

Fig. 1 Schematic illustration of the fabrication process and antitumor performance of AIO-EDTA NPs.

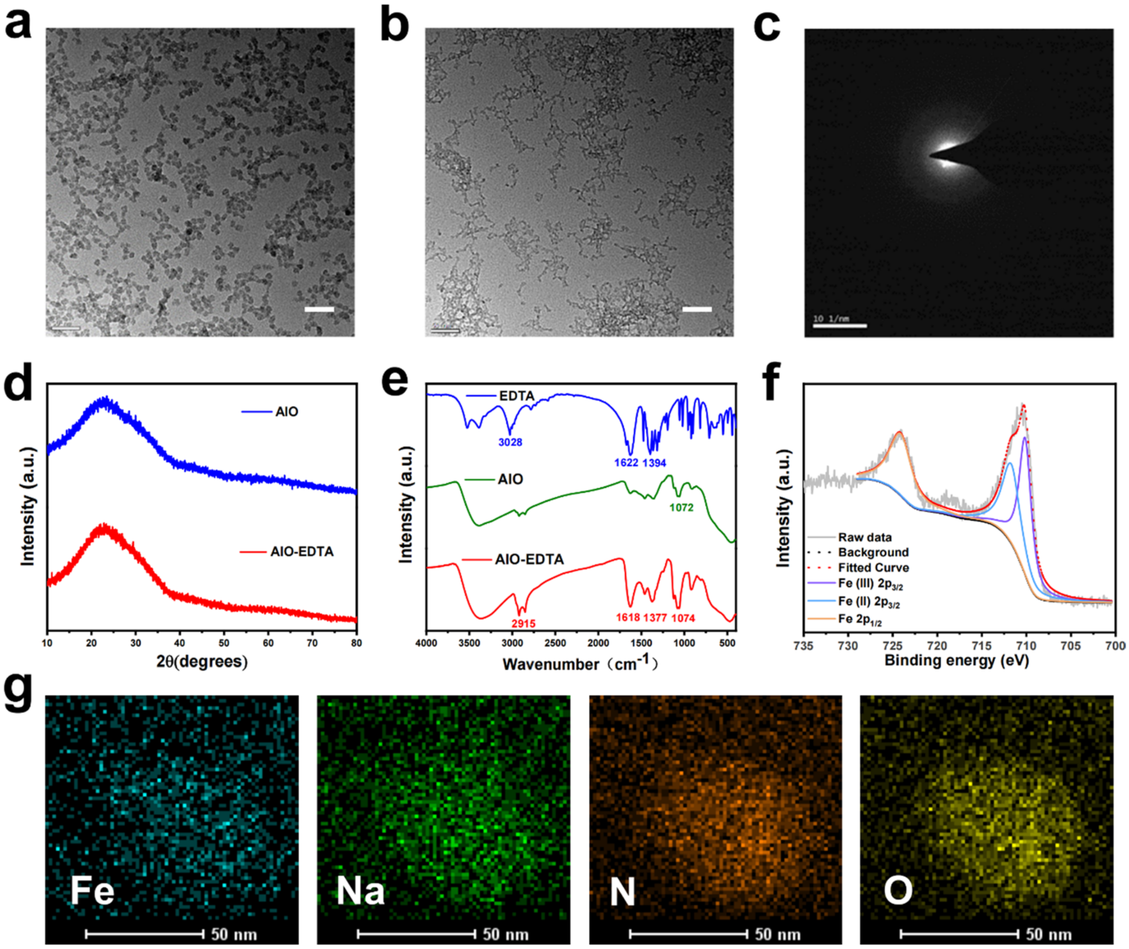

Fig. 2 Characterization of AIO and AIO-EDTA. (a) TEM image of AIO NPs; scale bar: 50 nm. (b) TEM image of AIO-EDTA NPs; scale bar: 50 nm. (c) Selected area electron diffraction (SAED) pattern of AIO NPs. (d) XRD patterns of AIO and AIO-EDTA NPs. (e) FTIR spectra of EDTA, AIO and AIO-EDTA. (f) Fe 2p spectrum of XPS spectra of AIO-EDTA. (g) Elemental mapping of AIO-EDTA NPs, including Fe, Na, N and O; scale bar: 50 nm.

transmission electron microscopy (TEM, Fig. 2a and b). However, the mean hydrodynamic diameter of AIO-EDTA (Fig. S1, ESI†) detected by dynamic light scattering (DLS) is about 180 nm. The synthesis of AIO with an amorphous structure can be verified by selected area electron diffraction (SAED, Fig. 2c) and X-ray diffraction (XRD, Fig. 2d).

The XRD patterns of AIO and AIO-EDTA show a broad peak near 25 degrees, which can be attributed to blank glass (Fig. S2, ESI†). Furthermore, the chemical valence of the obtained AIO and AIO-EDTA is evaluated using X-ray photoelectron spectroscopy (XPS, Fig. 2e and S3, ESI†). The binding energy peak positions of 724.3 eV and 710.8 eV correspond to the Fe $2p_{3/2}$ and Fe $2p_{1/2}$ species, respectively. The satellite peak observed in AIO at a position higher than 8.1 eV of the Fe $2p_{3/2}$ principal peak should be assigned to the Fe^{3+} species.[29,30] In contrast to AIO, the split Fe(II) $2p_{3/2}$ peak signal of AIO-EDTA is significantly enhanced, and the satellite peak disappears, indicating that the proportion of Fe(II) is enhanced. In addition, the successful loading of EDTA into AIO can be verified by the appearance of Na 1S peaks in the high-resolution XPS spectrum. We further verified the successful loading of EDTA by Fourier transform infrared spectroscopy (FTIR, Fig. 2f) and elemental mapping (Fig. 2g). Through inductively coupled plasma-mass spectrometry (ICP-MS), the content of Na could be determined to be 1 wt%, and the EDTA loading efficiency was up to 7.5 wt%. In order to enhance physiological stability and biocompatibility, AIO-EDTA NPs were modified with PEG. The successful PEGylation of AIO-EDTA is confirmed using the zeta potential, which changes between bare AIO-EDTA NPs (23.97 ± 0.97 mV) and AIO-EDTA-PEG NPs (40.17 ± 2.43 mV) (Fig. S4, ESI†). The hydrodynamic sizes of AIO-EDTA-PEG are higher than those of AIO-EDTA, which could help to prove successful PEG modification. Moreover, Fe^{3+} and EDTA release experiment was explored by incubating AIO-EDTA in phosphate-buffered saline (PBS) solutions with pH 5.5 and 7.4 (Fig. S5, ESI†). As intended, because of the acidolysis of Fe_2O_3, 91.9% of iron ions and 82.2% of EDTA were released at pH 5.5 within 24 h, respectively. Nevertheless, only 35.3% of iron ions and 29.5% of EDTA were released at pH 7.4 within 24 h, respectively, which indicated that the NPs have high acidity-responsive degradability.

In vitro evaluation of chemodynamic therapy performance

To verify our hypothesis that AIO-EDTA NPs have a better catalytic activity in the Fenton reaction, we used electron spin resonance (ESR) to measure the $^{\bullet}$OH generation in AIO, AIO-EDTA or AIO mixed with EDTA in an acidic environment. As shown in Fig. 3a, AIO-EDTA NPs generate stronger $^{\bullet}$OH signal peaks than AIO, demonstrating the enhanced Fenton reaction performance. This is attributed to the chelate complex of Fe^{3+}/Fe^{2+} with EDTA reducing the redox potential of Fe^{3+}/Fe^{2+} from 0.77 V to 0.209 V (*vs.* NHE), which enhanced the thermodynamic driving force of the Fenton reaction and demonstrated that the reduction of Fe^{3+}/Fe^{2+}-EDTA might be realized through $O_2^{\bullet-}$ rather than H_2O_2.[12,31,32] It is worth mentioning that AIO-EDTA showed higher Fenton reaction performance than the mixed group of AIO and EDTA, which may be attributed to the dissolution of more iron ions from AIO-EDTA NPs. Furthermore, 3,3′,5,5′-tetramethylbenzidine (TMB)-H_2O_2 colorimetric experimental results also show almost no color change with AIO, whereas the color turned dark blue with AIO-EDTA, illustrating that EDTA enhanced the Fenton reaction activity of AIO (Fig. 3b and S6, ESI†).

In vitro regulation of Ca^{2+} concentration by AIO-EDTA

To explore the chelation of our materials with Ca^{2+} ions in the TME, we used RPMI 1640 as the simulated environment to detect by ICP the Ca^{2+} concentration in the solution before and after adding AIO-EDTA. The significant decrease in Ca^{2+} concentration indicates that EDTA can chelate with Ca^{2+} in the tumor microenvironment (Fig. 3c). Then, the intracellular Ca^{2+} concentrations in 4T1 cells were measured using the Fluo-4 fluorescent probe and the extracellular Ca^{2+} concentrations were measured by ICP. As shown in Fig. 3d and S7 (ESI†), there was no significant difference in the extracellular Ca^{2+} concentration, but the intracellular Ca^{2+} concentration in AIO-EDTA NP-treated group was obviously higher than that of other groups. The above phenomenon is believed to be due to the chelation of AIO-EDTA NPs with intracellular calcium ions, leading to the release of calcium ions from organelles. It should be noted that there was no significant change of intracellular Ca^{2+} concentration in the EDTA group because EDTA chelates with Ca^{2+} at the cell surface, making it difficult for EDTA to enter the cells.

To verify that EDTA could induce cell separation, 4T1 cells were incubated with PBS, EDTA, AIO or AIO-EDTA for 1 h, and the morphological changes of cells were further observed using a microscope. It was observed that in the control group, the untreated cells attached to the container wall were spindle-shaped and the connections between cells were good, while the cells in the EDTA group and the AIO-EDTA group had changes in the cell morphology and the connections between cells were destroyed (Fig. 3e). Moreover, the expression of

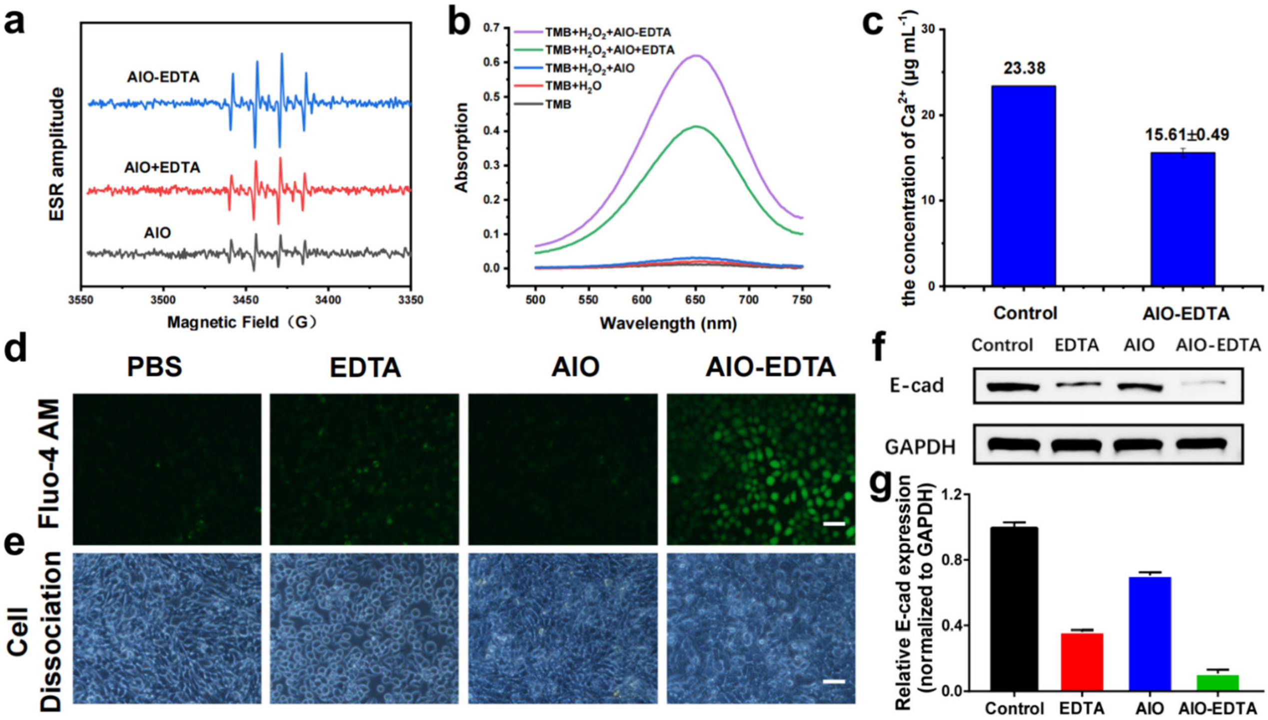

Fig. 3 (a) ESR spectra of AIO NPs, AIO NPs with EDTA-2Na, and AIO-EDTA NPs in the presence of H_2O_2 at pH 5.5. 5,5-Dimethyl-1-pyrroline N-oxide (DMPO) was used as the spin trap agent. (b) UV-Vis spectra of TMB under different conditions. (c) Ca^{2+} concentration in RPMI 1640 before and after adding AIO-EDTA NPs. (d) The intracellular Ca^{2+} concentration of 4T1 cells treated with RPMI 1640, EDTA, AIO NPs and AIO-EDTA NPs; scale bar: 20 μm. (e) Microphotographs of 4T1 cells after being treated with RPMI 1640, EDTA, AIO NPs and AIO-EDTA NPs for 1 h; scale bar: 20 μm. (f) The E-cadherin protein expressions of the tumors that received the treatments. (g) The corresponding quantitative levels of E-cadherin protein expressions.

E-cad was further evaluated by western blotting (WB). The results show that the protein contents of EDTA and AIO-EDTA groups displayed an evident decline compared with the control and AIO groups (Fig. 3f and g).

Cellular anticancer efficiency evaluation of AIO-EDTA NPs

In order to evaluate the anticancer efficiency and specificity of AIO-EDTA NPs, a standard methyl thiazolyl tetrazolium (MTT) assay was performed on 4T1 cells and noncancerous mouse fibroblast cells (L929), respectively. Compared to EDTA and AIO alone, the AIO-EDTA group shows the strongest therapeutic effect on 4T1 cells, which is due to the combination of IIT and chelation-enhanced CDT (Fig. 4a and b). Nevertheless, AIO-EDTA NPs show no obvious cytotoxicity effects on L929 cells after 24 h of cultivation at the corresponding concentrations (Fig. S8, ESI†). Next, the degree of oxidative stress in the cancer cells was investigated by incubating 4T1 cells with the ROS fluorescent probe 2′,7′-dichlorofluorescein diacetate (DCFH-DA) after different treatments. No evident green fluorescence was observed in 4T1 cells of the control group and EDTA-treated group, while AIO NPs could trigger obvious green fluorescence emission from 4T1 cells (Fig. 4c and S9, ESI†). Noticeably, the AIO-EDTA-treated group was capable of triggering the strongest fluorescence emission from 4T1 cells, illustrating that AIO-EDTA is effective in motivating prooxidation reactions in cancer cells and consequently triggering oxidative stress. Furthermore, the increase of ROS can lead to lysosomal membrane permeabilization (LMP), which usually

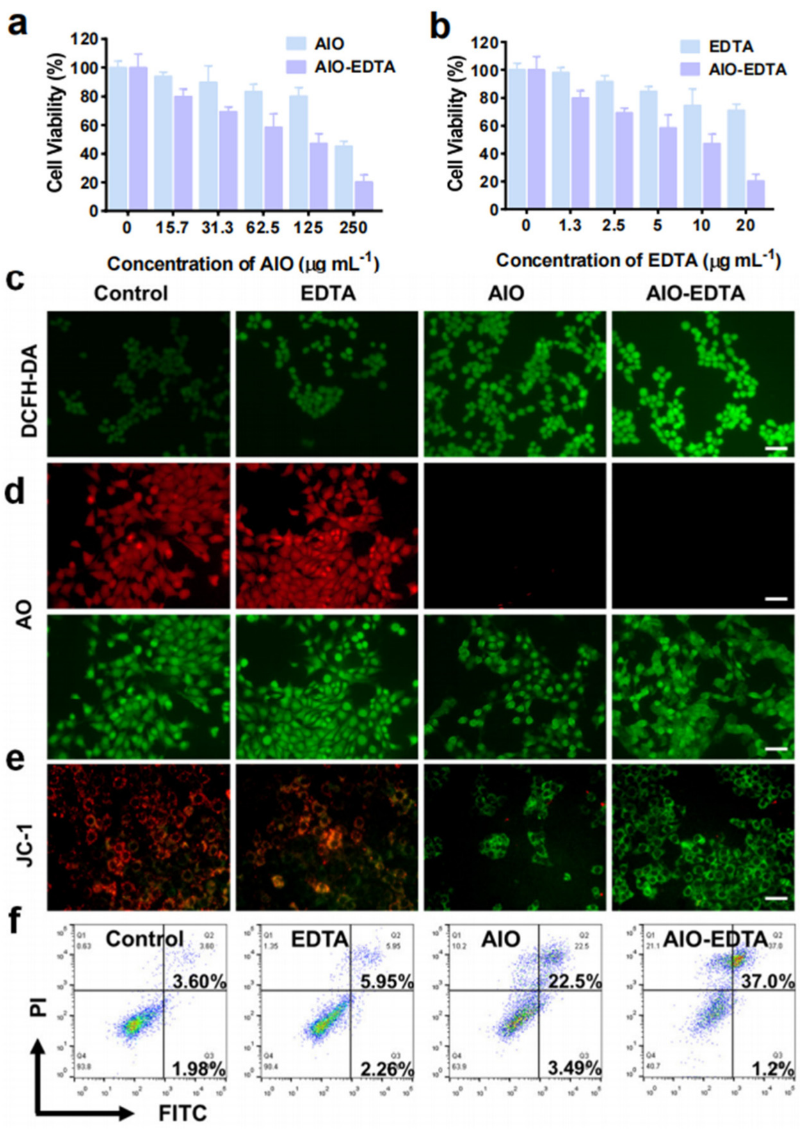

Fig. 4 (a) Relative cell viability of 4T1 cells treated with AIO NPs or AIO-EDTA NPs at different concentrations. (b) Relative cell viability of 4T1 cells treated with EDTA or AIO-EDTA NPs at different concentrations. (c) Detection of ROS at the cellular level; scale bar is 20 μm. (d) The measurement of lysosomal membrane integrity; scale bar is 20 μm. (e) Mitochondrial membrane potential measurement; scale bar is 20 μm. (f) Flow cytometry investigation of the apoptotic mechanism of annexin V-FITC/PI-stained 4T1 cells after different treatments for 24 h.

occurs at the early stage of apoptosis.[33] The almost complete disappearance of red fluorescence in the AIO and AIO-EDTA groups as observed by acridine orange (AO) staining assay indicates the loss of endosomal membrane integrity (Fig. 4d).[34] Similarly, the decrease of mitochondrial membrane potential (MMP) is a hallmark event of apoptosis, which can be detected using the JC-1 probe. The change of mitochondrial membrane potential from high to low was accompanied by the transition of the JC-1 probe from J-aggregates (red) to monomers (green). As shown in Fig. 4e and S10 (ESI†), 4T1 cells in the AIO-EDTA group displayed the strongest green fluorescence, indicating the lowest mitochondrial membrane potential. To quantitatively observe the therapeutic effects of different treatments, we performed a live–dead cell staining assay and flow cytometry analysis, which further confirmed that AIO-EDTA caused the most severe cell apoptosis (Fig. 4f).

In vivo tumor therapy with AIO-EDTA NPs

Subsequently, to explore the anti-tumor efficiency of AIO-EDTA NPs *in vivo*, a 4T1 xenograft tumor model was established using BALB/c mice. As shown in Fig. 5a, the tumor-bearing mice were randomly divided into four groups (n = 5 in each group), followed by tail intravenous injection with (i) saline (control group), (ii) EDTA, (iii) AIO NPs and (iv) AIO-EDTA NPs on day 0 and 5, respectively. A significant enhancement of the tumor volume was observed in the control group (Fig. 5c, d and S11, ESI†), while EDTA and AIO groups displayed a certain degree of inhibition. By comparison, conspicuous tumor growth inhibition could be observed in the AIO-EDTA group, which should be ascribed to the combination of IIT and chelation-enhanced CDT. Of note, there was no significant trend in the body weight of the mice in each group and no damage was

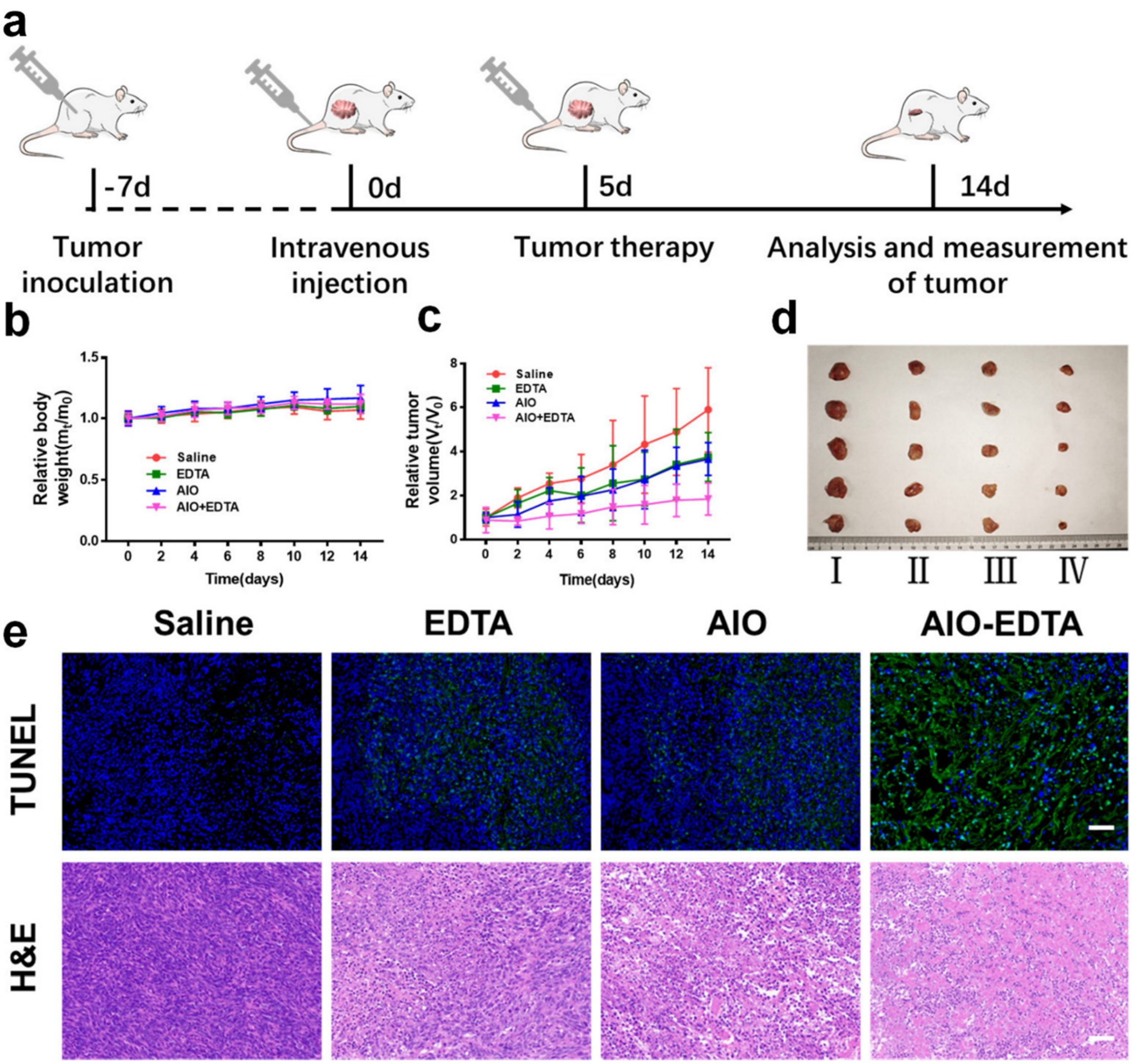

Fig. 5 (a) Schedule of animal experiment procedures. (b) Relative body weight changes during various treatments. (c) Variation curves of relative tumor volume. (d) The photo of excised tumors after 14 days of different treatments. (e) Histochemical analyses (TUNEL and H&E) of 4T1 tumor tissues harvested from mice after different treatments on day 14; scale bar is 20 μm.

observed in the major organs (heart, liver, spleen, lung, and kidney) of the mice during the treatment period, indicating the excellent biocompatibility of AIO-EDTA (Fig. 5b and S12, ESI†). Furthermore, terminal-deoxynucleotidyl-transferase-mediated nick end labeling (TUNEL) and hematoxylin and eosin (H&E) staining of tumor tissue were applied to verify the anticancer effect of AIO-EDTA. As shown in Fig. 5e, the strongest green fluorescence of the AIO-EDTA group demonstrated the most extensive cancer cell apoptosis among all groups. Correspondingly, the pathological H&E staining indicated that tumor structures were severely damaged in the AIO-EDTA NP group after treatments. This observation suggests that AIO-EDTA NPs can achieve effective anti-tumor function by the combination of IIT and chelation-enhanced CDT.

Conclusions

In summary, an effective nanomedicine based on chelation was designed for the combined treatment with IIT and CDT. The CDT efficiency was increased by introducing EDTA, which formed an Fe chelating complex to reduce the activation energy of the Fenton reaction. Furthermore, EDTA chelated Ca^{2+} from E-cadherin for induction of tumor cell separation, and EDTA chelated with intracellular Ca^{2+} to release endogenous Ca^{2+} from organelles, which affected the normal physiological activities of cancer cells. Both *in vitro* and *in vivo* antitumor experiments further certified the biocompatibility and biosafety of AIO-EDTA NPs, as well as they can effectively inhibit tumor growth. We believe that chelation has great potential in cancer therapy, and this study provides a new way to design efficient Fenton reaction catalysts.

Conflicts of interest

There are no conflicts to declare.

Acknowledgements

This work is financially supported by the Science and Technology Development Planning Project of Jilin Province (20220508089RC), the National Natural Science Foundation of China (Grant No. NSFC 51929201 and 52102354), the Postdoctoral Innovative Talents Support Program (BX2021360), the Project funded by the China Postdoctoral Science Foundation (2021M703130 and 2021M691919), the Special Health Project of Jilin Province (2020SCZT010) and the Guangdong Provincial Natural Science Foundation of China (No. 2018A030313355). All animal procedures were performed in accordance with the Guidelines for Care and Use of Laboratory Animals of Jilin University and approved by the Institutional Animal Care and Use Committee of Jilin University.

References

1 R. L. Siegel, K. D. Miller, N. S. Wagle and A. Jemal, *CA Cancer J. Clin.*, 2023, **73**, 17–48.
2 H. Sung, J. Ferlay, R. L. Siegel, M. Laversanne, I. Soerjomataram, A. Jemal and F. Bray, *CA Cancer J. Clin.*, 2021, **71**, 209–249.
3 C. Zhang, W. Bu, D. Ni, S. Zhang, Q. Li, Z. Yao, J. Zhang, H. Yao, Z. Wang and J. Shi, *Angew. Chem., Int. Ed.*, 2016, **55**, 2101–2106.
4 Z. Tang, Y. Liu, M. He and W. Bu, *Angew. Chem., Int. Ed.*, 2019, **58**, 946–956.
5 Q. Sun, Z. Wang, B. Liu, F. He, S. Gai, P. Yang, D. Yang, C. Li and J. Lin, *Coord. Chem. Rev.*, 2022, **451**, 214267.
6 C. Liu, Y. Cao, Y. Cheng, D. Wang, T. Xu, L. Su, X. Zhang and H. Dong, *Nat. Commun.*, 2020, **11**, 1735.
7 P. An, F. Fan, D. Gu, Z. Gao, A. M. S. Hossain and B. Sun, *J. Controlled Release*, 2020, **321**, 734–743.
8 Y. Hao, Z. Dong, M. Chen, Y. Chao, Z. Liu, L. Feng, Y. Hao, Z. L. Dong, M. C. Chen, Y. Chao, Z. Liu and L. Z. Feng, *Biomaterials*, 2020, **228**, 119568.
9 Y. Liu, S. Zhai, X. Jiang, Y. Liu, K. Wang, C. Wang, M. Zhang, X. Liu and W. Bu, *Adv. Funct. Mater.*, 2021, **31**, 2010390.
10 B. Yang and J. Shi, *J. Am. Chem. Soc.*, 2020, **142**, 21775–21785.
11 B. Yang, H. Yao, H. Tian, Z. Yu, Y. Guo, Y. Wang, J. Yang, C. Chen and J. Shi, *Nat. Commun.*, 2021, **12**, 3393.
12 N. Wang, L. Zhu, M. Lei, Y. She, M. Cao and H. Tang, *ACS Catal.*, 2011, **1**, 1193–1202.
13 L. Zhou, J. Chen, R. Li, L. Wei, H. Xiong, C. Wang, K. Chai, M. Chen, Z. Zhu, T. Yao, Y. Lin, C. Dong and S. Shi, *Small*, 2021, **17**, e2103919.
14 R. Banavath, R. Srivastava and P. Bhargava, *Mater. Chem. Phys.*, 2021, **267**, 124593.
15 H. F. Wang, X. Chen, F. Feng, X. Ji and Y. Zhang, *Chem. Sci.*, 2018, **9**, 8923–8929.
16 W. Wu, L. Yu, Q. Jiang, M. Huo, H. Lin, L. Wang, Y. Chen and J. Shi, *J. Am. Chem. Soc.*, 2019, **141**, 11531–11539.
17 W. Wu, L. Yu, Y. Pu, H. Yao, Y. Chen and J. Shi, *Adv. Mater.*, 2020, **32**, 2000542.
18 P. Zhao, Z. Tang, X. Chen, Z. He, X. He, M. Zhang, Y. Liu, D. Ren, K. Zhao and W. Bu, *Mater. Horiz.*, 2019, **6**, 369–374.
19 T. T. Shen, X. M. Li, Y. F. Tang, J. Wang, X. Yue, J. B. Cao, W. Zheng, D. B. Wang and G. M. Zeng, *Water Sci. Technol.*, 2009, **60**, 761–770.
20 M. Li, Q. Bao, J. Guo, R. Xie, C. Shen, Q. Wei, P. Hu, H. Qin and J. Shi, *Nano Lett.*, 2022, **22**, 2769–2779.
21 Q. Bao, P. Hu, W. Ren, Y. Guo and J. Shi, *Chem*, 2020, **6**, 2283–2299.
22 W. Li, A. L. Sabater, Y. T. Chen, Y. Hayashida, S. Y. Chen, H. He and S. C. Tseng, *Invest. Ophthalmol. Visual Sci.*, 2007, **48**, 614–620.
23 P. Zheng, B. Ding, G. Zhu, C. Li and J. Lin, *Angew. Chem., Int. Ed.*, 2022, **61**, 202204904.

24 Y. Li, S. Zhou, H. Song, T. Yu, X. Zheng and Q. Chu, *Biomaterials*, 2021, **277**, 121080.

25 J. An, M. Liu, L. Zhao, W. Lu, S. Wu, K. Zhang, J. Liu, Z. Zhang and J. Shi, *Adv. Funct. Mater.*, 2022, **32**, 2201275.

26 Y. Liu, M. Zhang and W. Bu, *View*, 2020, **1**, e18.

27 B. Ding, P. Zheng, D. Li, M. Wang, F. Jiang, Z. Wang, P. Ma and J. Lin, *Nanoscale*, 2021, **13**, 10906–10915.

28 Y. Liu, X. Ji, W. W. L. Tong, D. Askhatova, T. Yang, H. Cheng, Y. Wang and J. Shi, *Angew. Chem., Int. Ed.*, 2018, **57**, 1510–1513.

29 T. Yamashita and P. Hayes, *Appl. Surf. Sci.*, 2008, **254**, 2441–2449.

30 L. Feng, S. Gai, F. He, P. Yang and Y. Zhao, *ACS Nano*, 2020, **14**, 7245–7258.

31 T. J. Strathmann and A. T. Stone, *Environ. Sci. Technol.*, 2002, **36**, 5172–5183.

32 Z. Wang, Y. Du, P. Zhou, Z. Xiong, C. He, Y. Liu, H. Zhang, G. Yao and B. Lai, *Chem. Eng. J.*, 2023, **454**, 140096.

33 H. D. Ulf, T. Brunk, K. Roberg and H. B. Hellquist, *Free Radical Biol. Med.*, 1997, **2**, 616–626.

34 L.-S. Lin, T. Huang, J. Song, X.-Y. Ou, Z. Wang, H. Deng, R. Tian, Y. Liu, J.-F. Wang, Y. Liu, G. Yu, Z. Zhou, S. Wang, G. Niu, H.-H. Yang and X. Chen, *J. Am. Chem. Soc.*, 2019, **141**, 9937–9945.